Optimizing Bi Active Sites by Ce Doping for Boosting Formate-Production in A Wide Potential Window

Yi-Cheng Wang[1], Peng-Fei Sui[1], Chenyu Xu[2], Meng-Nan Zhu[1], Renfei Feng[3], Hongtao Ma,[1] Hongbo Zeng,[1] Xiaolei Wang[1,*], Jing-Li Luo[1,4,*]

[1] Department of Chemical and Materials Engineering, University of Alberta, 9211-116 Street NW., Edmonton, Alberta T6G 1H9, Canada

[2] State Key Laboratory of Clean Energy Utilization, Zhejiang University, Hangzhou 310027, P.R. China

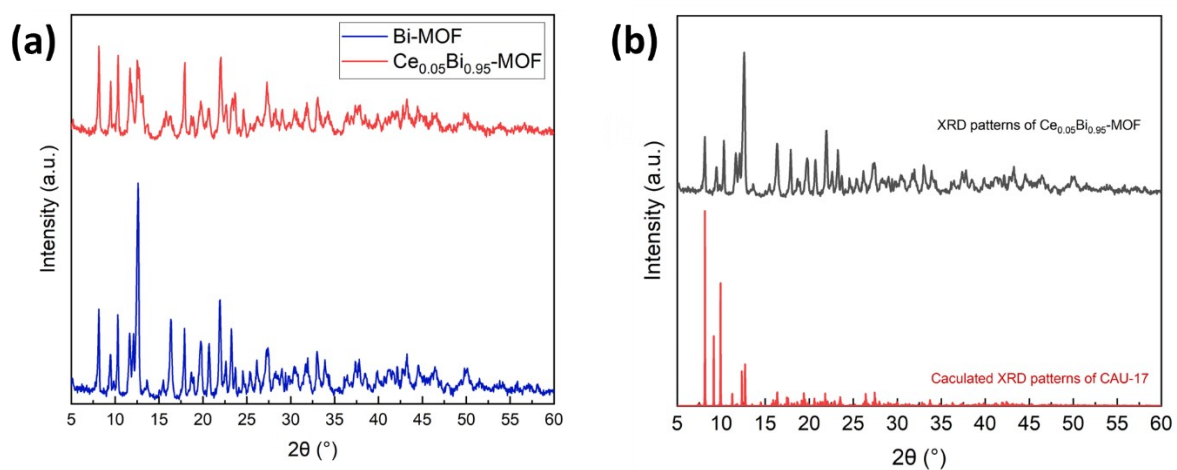[3] Canadian Light Source Inc., 44 Innovation Boulevard, Saskatoon, Saskatchewan S7N 0X4, Canada

[4] Department of Materials Science and Engineering, Shenzhen University, Shenzhen 518060, P.R. China
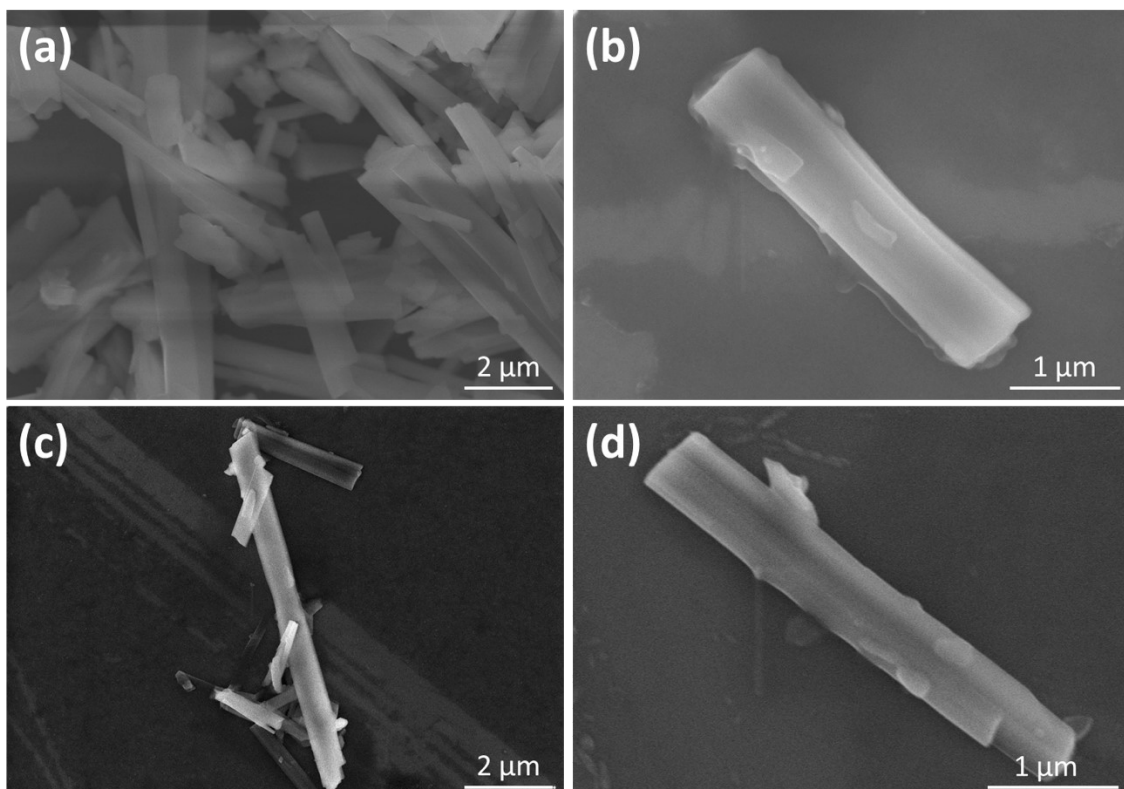
Y. Wang and P. Sui contributed equally to this work.

Corresponding authors:
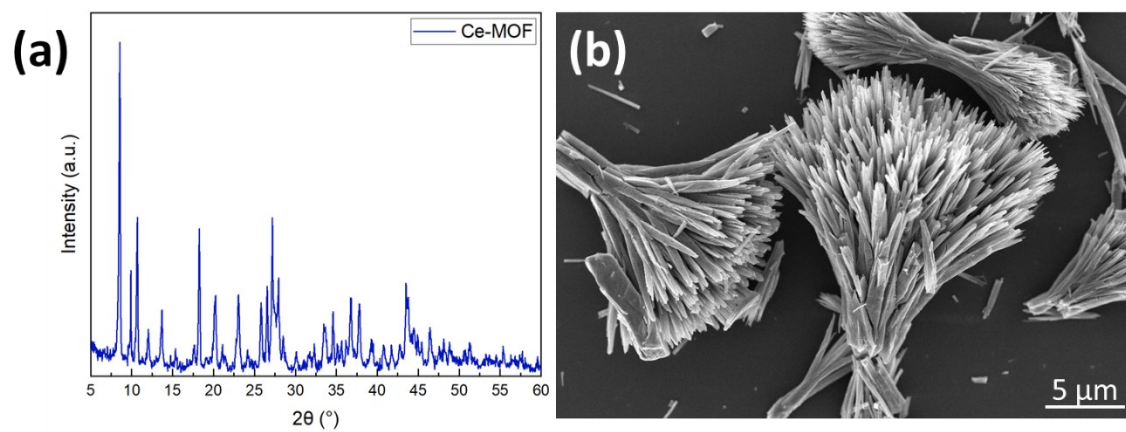
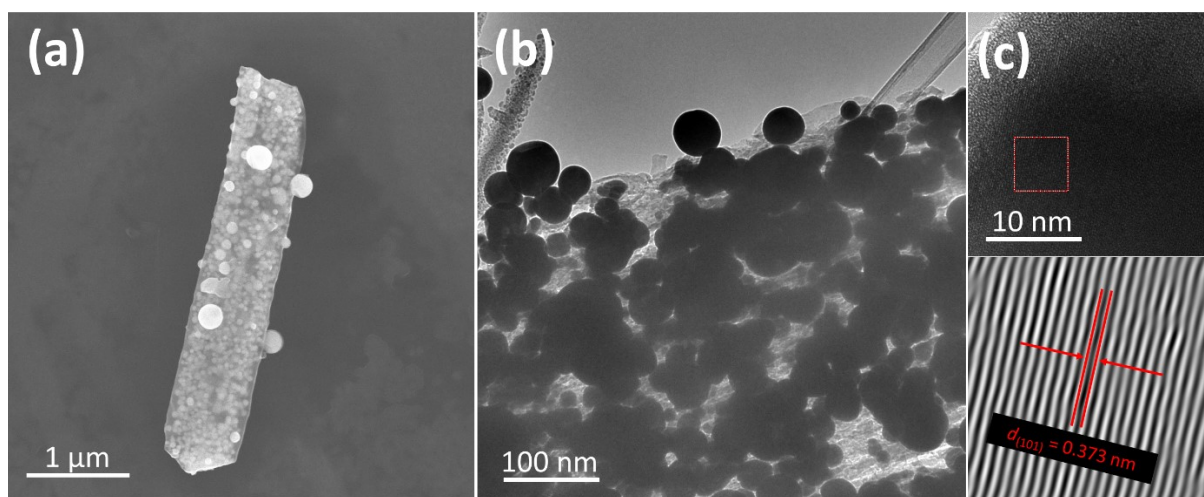Xiaolei Wang, email: xiaolei.wang@ualberta.ca

Jingli Luo, email: jingli.luo@ualberta.ca

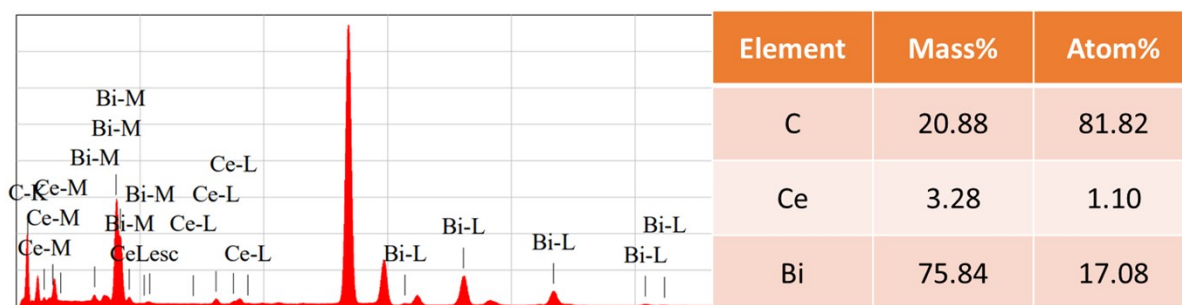**Figure S1.** XRD patterns of Bi-MOF and $Ce_{0.05}Bi_{0.95}$-MOF precursor.

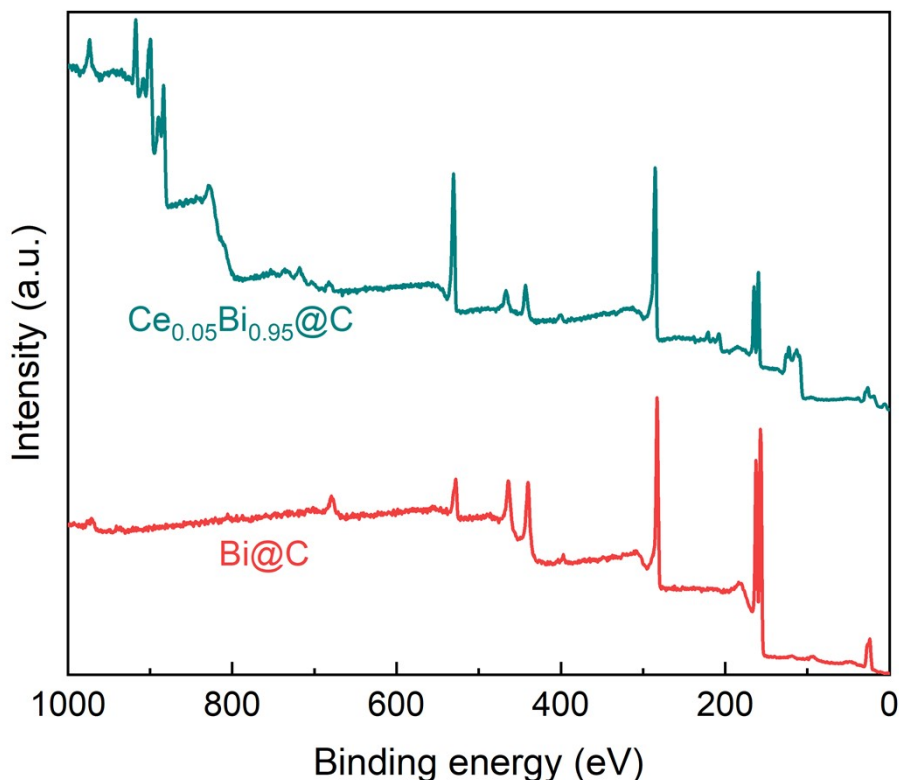**Figure S2.** SEM patterns of (a,b) Bi-MOF NRs and (c,d) $Ce_{0.05}Bi_{0.95}$-MOF NRs.

Figure S3. (a) XRD and (b) SEM patterns of Ce-MOF with broom-like structure.

Figure S4. (a) SEM and (b,c) TEM patterns of Bi@C NRs.

Element	Mass%	Atom%
C	20.88	81.82
Ce	3.28	1.10
Bi	75.84	17.08

Figure S5. Elemental mapping of $Ce_{0.05}Bi_{0.95}$@C NRs.

Figure S6. The full range XPS spectrum of Bi@C and $Ce_{0.05}Bi_{0.95}$@C NRs.

For the High-resolution XPS spectrum of Ce 3d of $Ce_{0.05}Bi_{0.95}$@C NRs, these peaks could be fitted into eight peaks that these four characteristic peaks (882.69 eV, 884.00 eV, 889.11 eV, and 898.73 eV) are ascribed to the Ce $3d_{5/2}$ and those two characteristic peaks (901.19 eV, 902.12 eV, 907.43 eV, and 917.14 eV) are assigned to the Ce $3d_{3/2}$. Specifically, the pair of peaks at 884.00 eV and 902.12 eV corresponds to Ce^{3+}, while the other peaks belong to Ce^{4+}. Therefore, the hybrid of Ce^{3+} and Ce^{4+} were introduced on the surface of 5% Ce-doped Bi@C NRs.
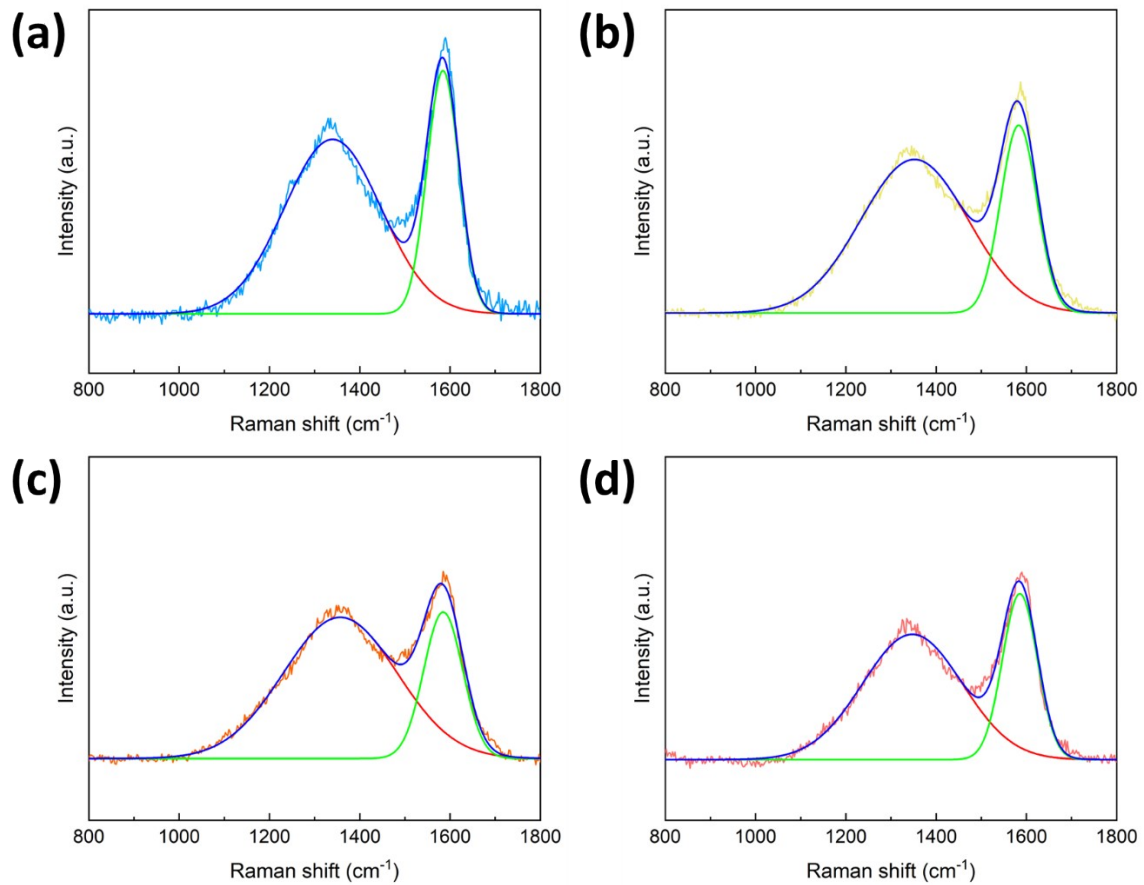
Figure S7. Raman spetra of (a) Bi@C NRs; (b) $Ce_{0.01}Bi_{0.99}$@C NRs; (c) $Ce_{0.05}Bi_{0.95}$@C NRs; (d) $Ce_{0.1}Bi_{0.9}$@C NRs.
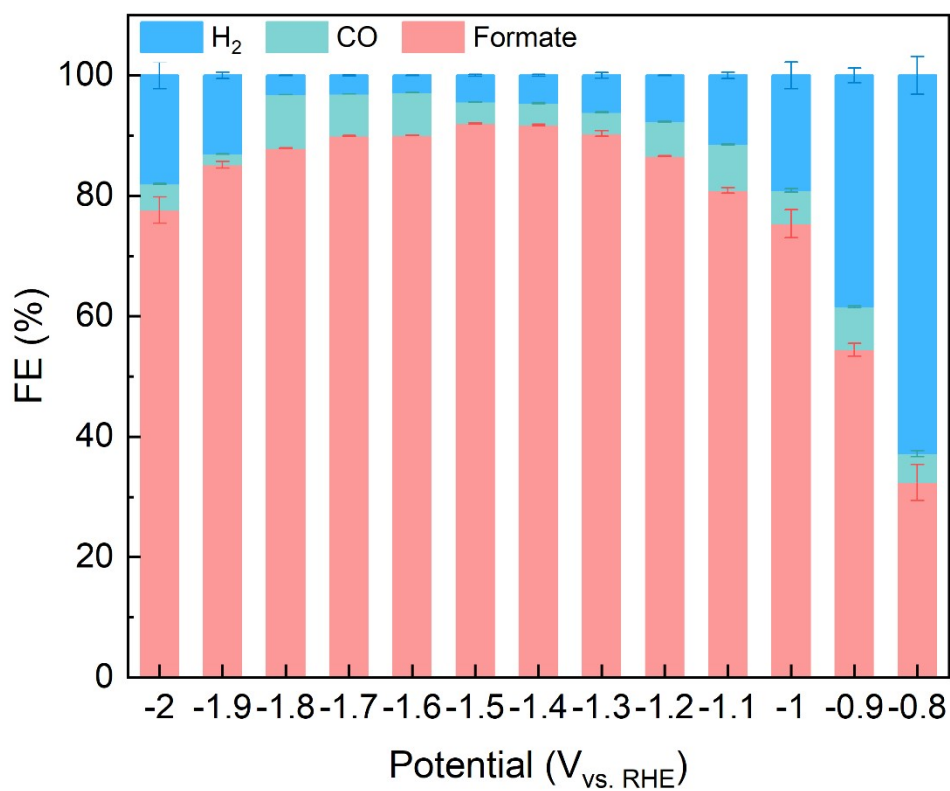
Figure S8. FEs of product distributions at different applied potentials on Bi@C.
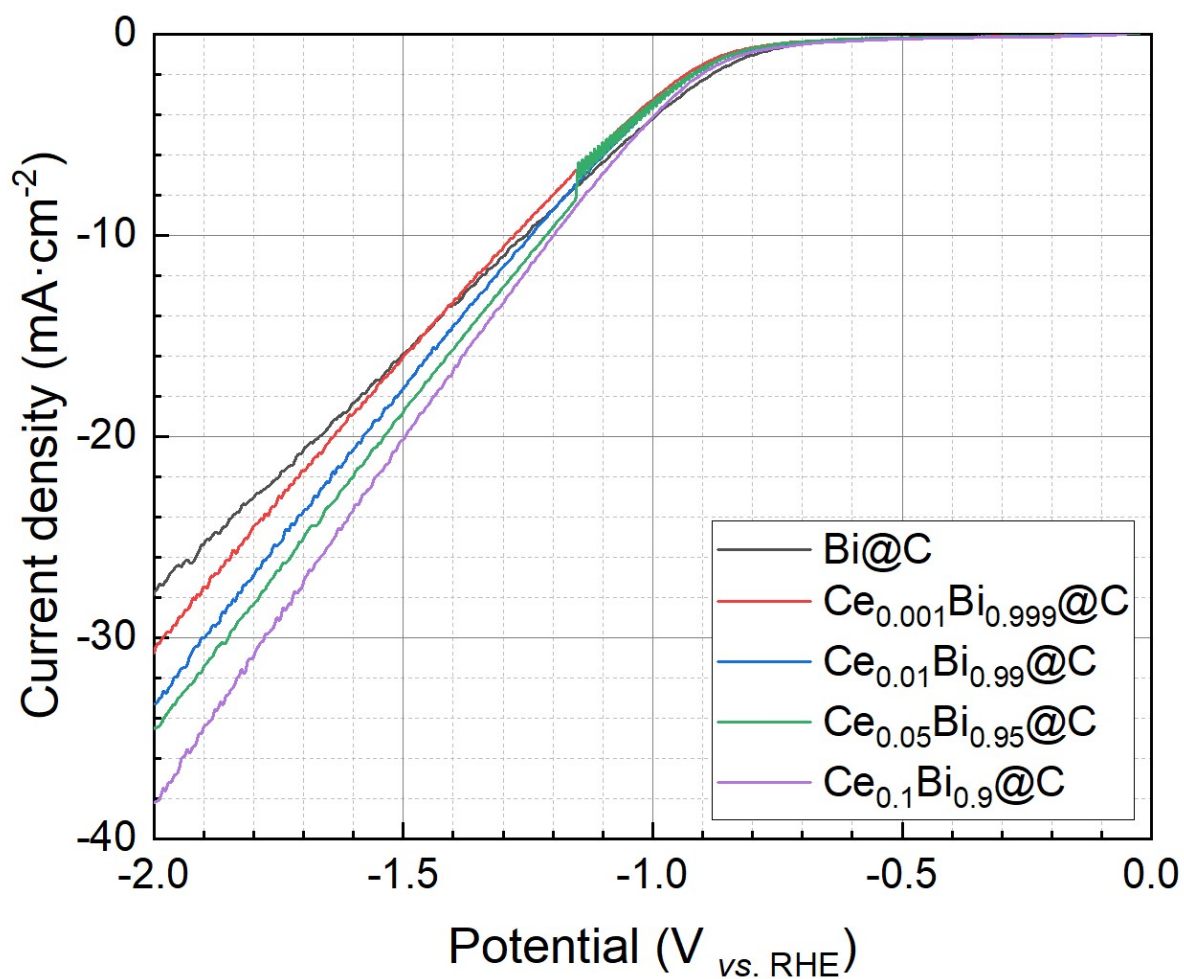
Figure S9. LSV curves of Bi@C NRs with different amounts of Ce doping in CO_2-saturated 0.1 M $KHCO_3$.
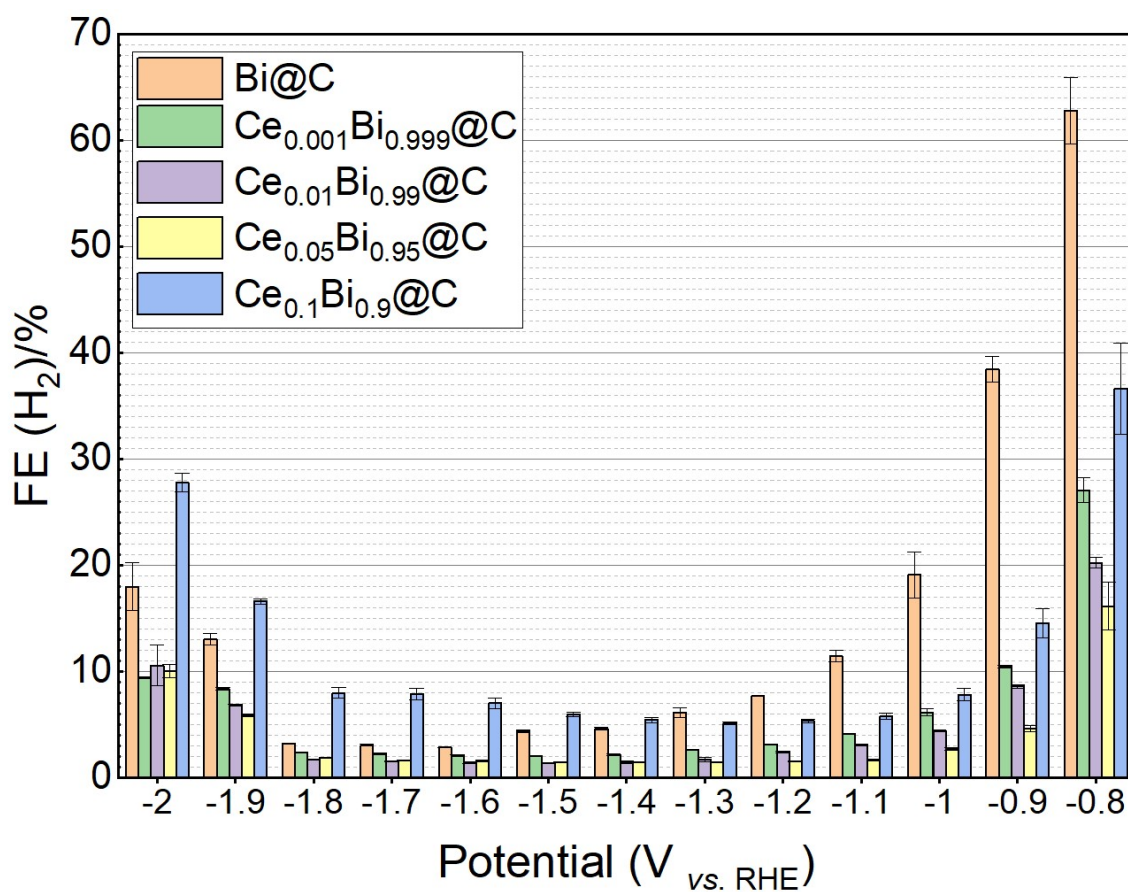
Figure S10. Fe$_{H2}$ of Bi@C NRs with different amounts of Ce doping at different applied potentials.
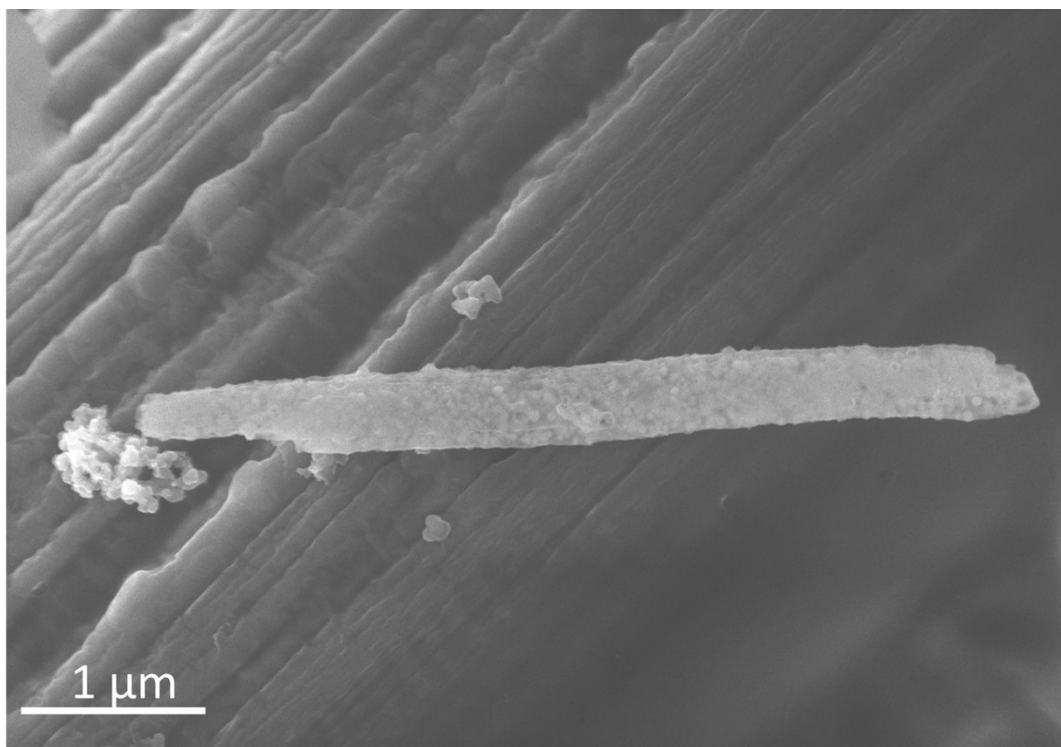
Figure S11. SEM image of $Ce_{0.05}Bi_{0.95}$@C NRs after stability test.

Figure S12. XRD pattern $Ce_{0.05}Bi_{0.95}@C$ NRs after stability test.

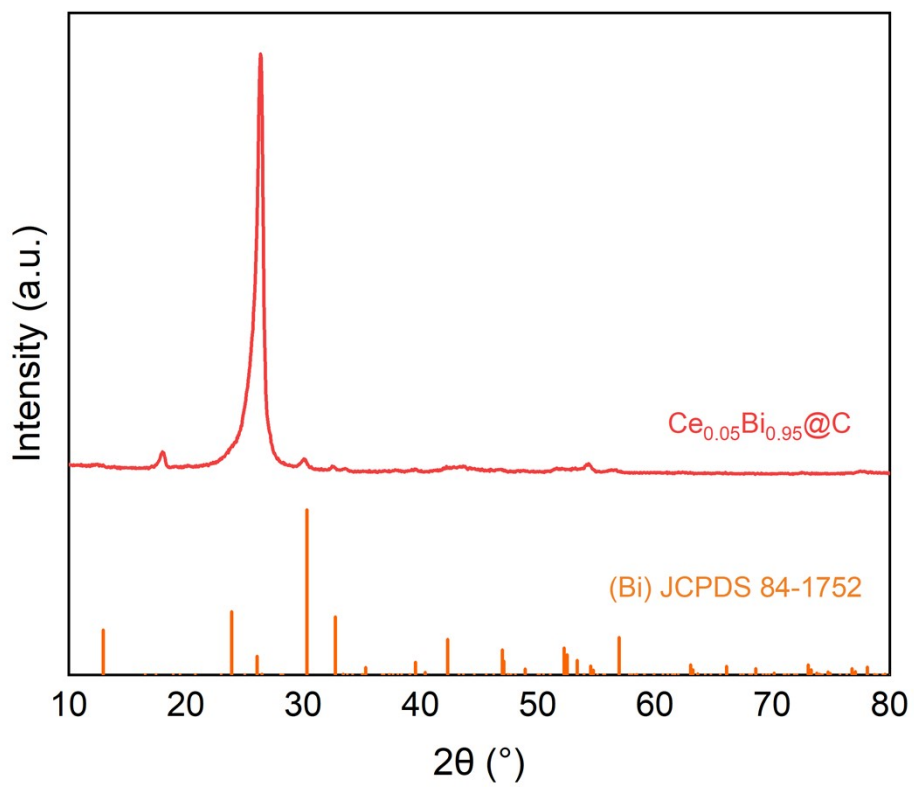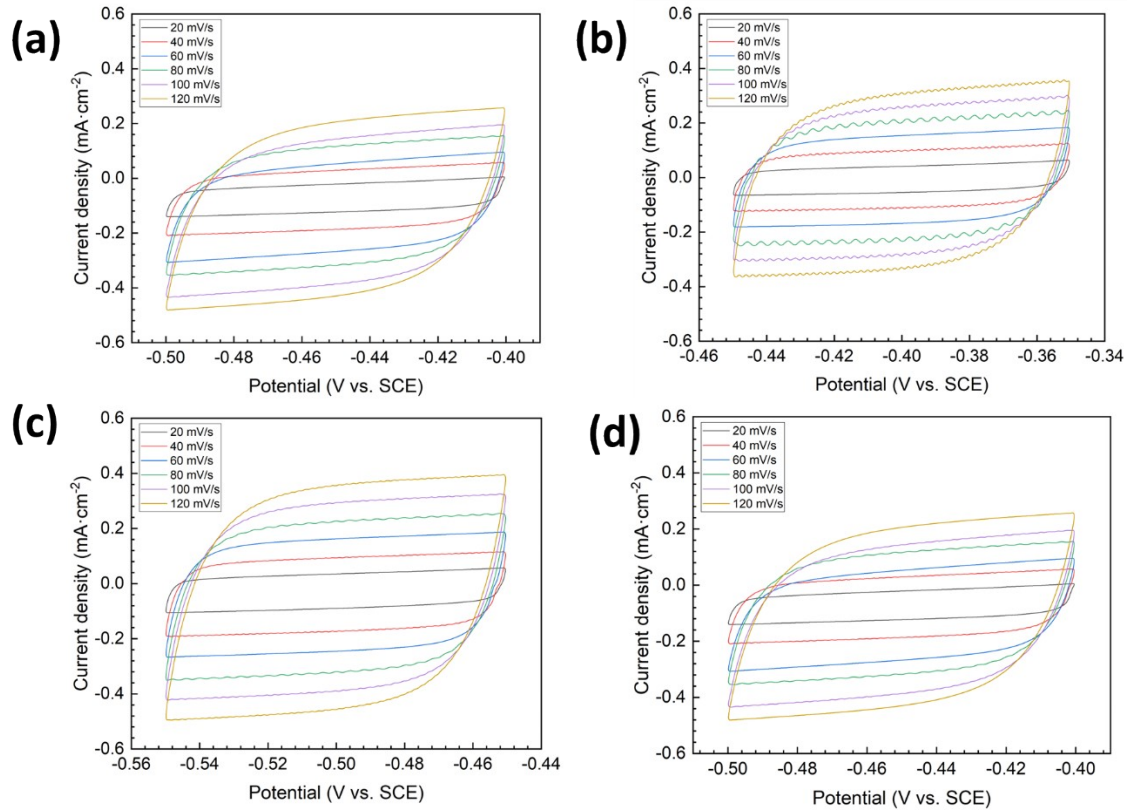**Figure S13.** CV curves of Bi@C NRs with different amounts of Ce doping.

Electrochemical active surface area (ECSA)

The ECSA of a material with similar composition is proportional to its electrochemical double-layer capacitance (C_{dl}), which is measured by CV in a non-Faradaic region at different scan rates (V_s) of 20, 40, 60, 80, 100, 120 mV s^{-1}. Then the double-layer capacitance (C_{dl}) was determined by plotting the $\Delta j=(j_a-j_c)$ at -0.5 V vs. SCE as a function of the scan rate. It can be calculated through the following equation:

$$C_{dl} = \frac{d(\Delta j)}{2dV_s}$$

The ECSA can be calculated from the C_{dl} according to:

$$ECSA = \frac{C_{dl}}{C_s}$$

Where C_s is the specific capacitance of a flat surface with 1 cm^2 of real surface area. Here, the average double-layer capacitance of a smooth metal surface is assumed to be 20 μF cm^{-2} [1]. The calculated value of ECSA for Bi@C NRs was about 10.19 cm^2, while the value for 1%, 5%, and 10% Ce-doped Bi@C NRs were 11.49 cm^2, 23.68 cm^2, and 26.75 cm^2, respectively. ECSA-corrected Tafel slopes for formate formation were calculated based on the corresponding ECSA-corrected formate partial current densities and overpotentials.
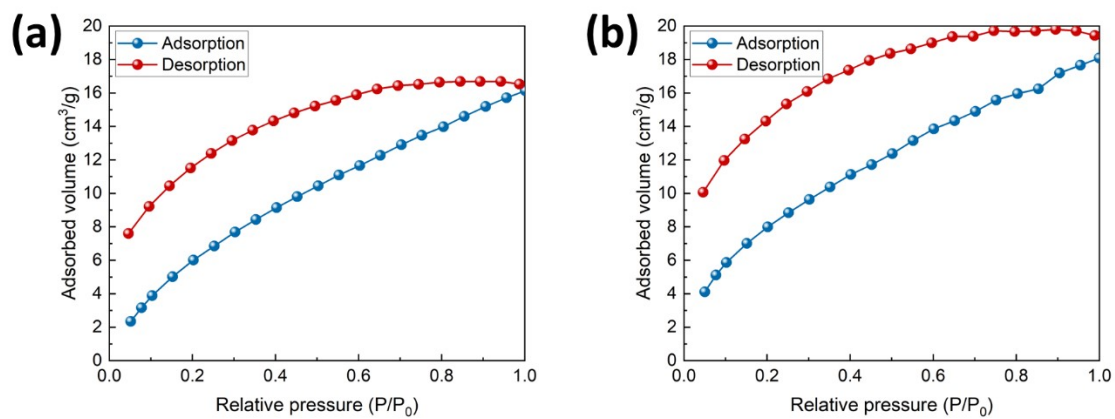
Figure S14. CO_2 adsorption isotherms of Bi@C NRs and $Ce_{0.05}Bi_{0.95}$@C NRs.
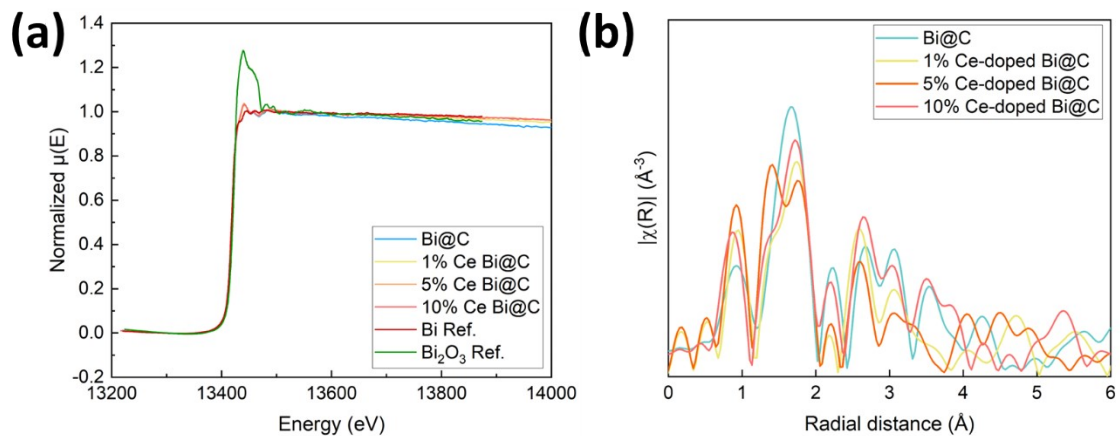
Figure S15. (a) XAS spectra of Bi@C and Ce-doped Bi@C NRs; (b) Fourier transforms of k^2-weighted EXAFS spectra to the R space of Bi@C and Ce-doped Bi@C NRs.
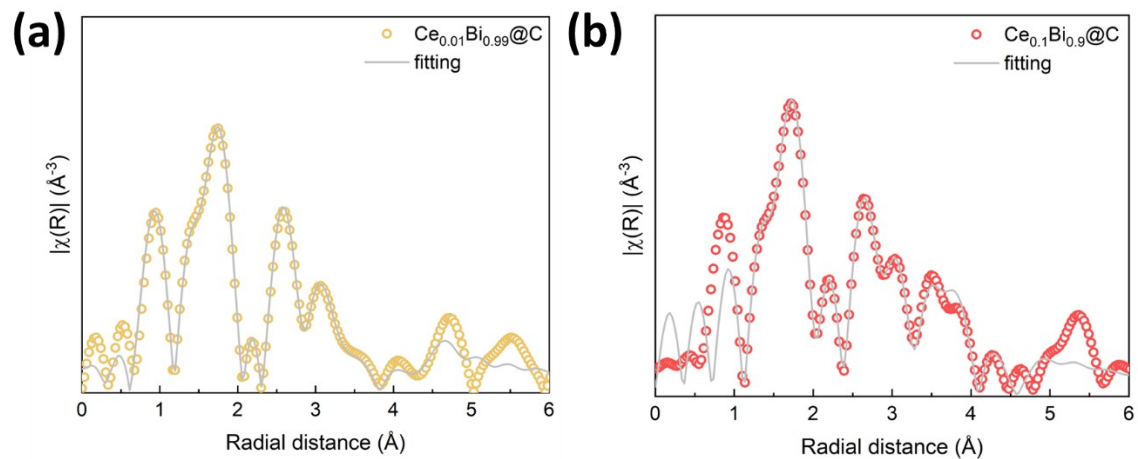
Figure S16. Representative fitting of the EXAFS spectra to the R-space of (a) $Ce_{0.01}Bi_{0.99}@C$ NRs; (b) $Ce_{0.1}Bi_{0.9}@C$ NRs.
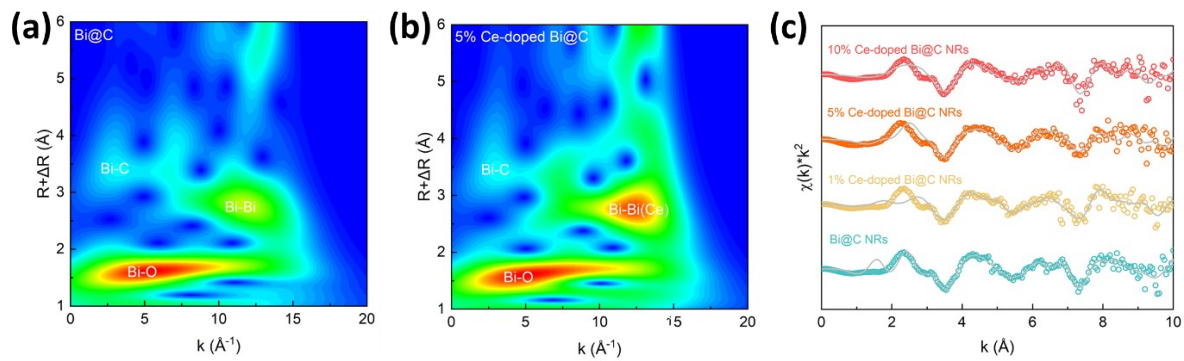
Figure S17. Morlet wavelet transform of EXAFS spectra in both *R*-space and *k*-space of (a) Bi@C NRs and (b) $Ce_{0.05}Bi_{0.95}@C$ NRs, respectively; (c) Fitting results of EXAFS spectra to *k*-space.
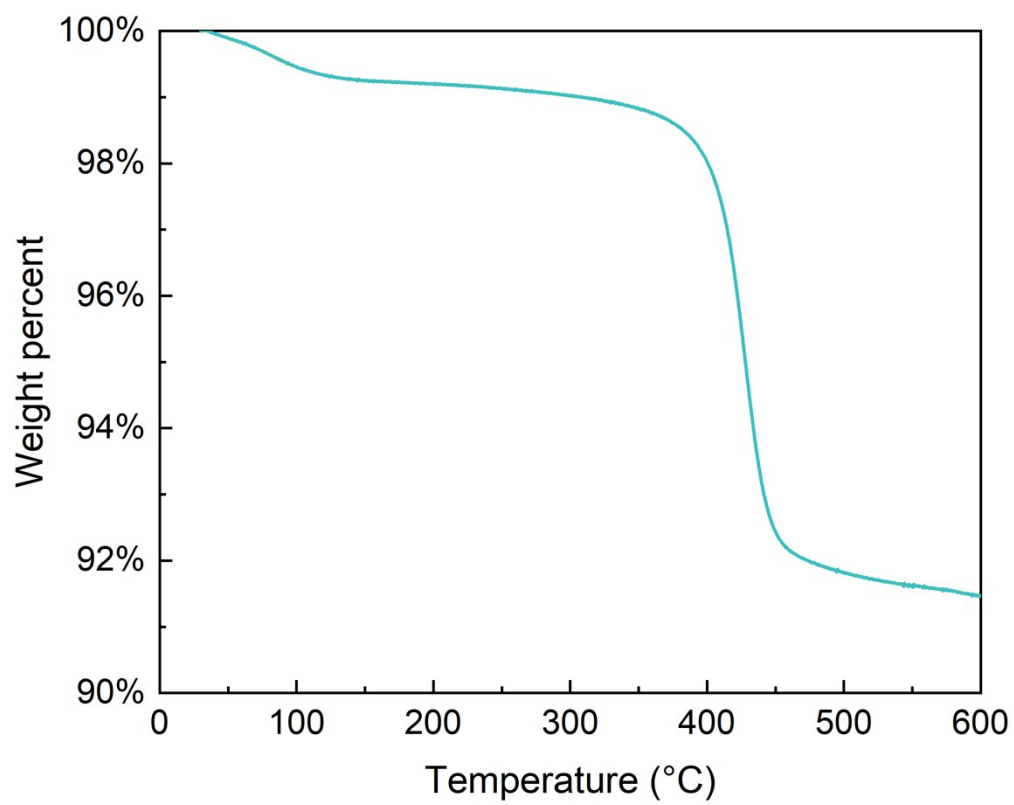
Figure S18. Thermogravimetric analysis of $Ce_{0.05}Bi_{0.95}@C$ NRs.
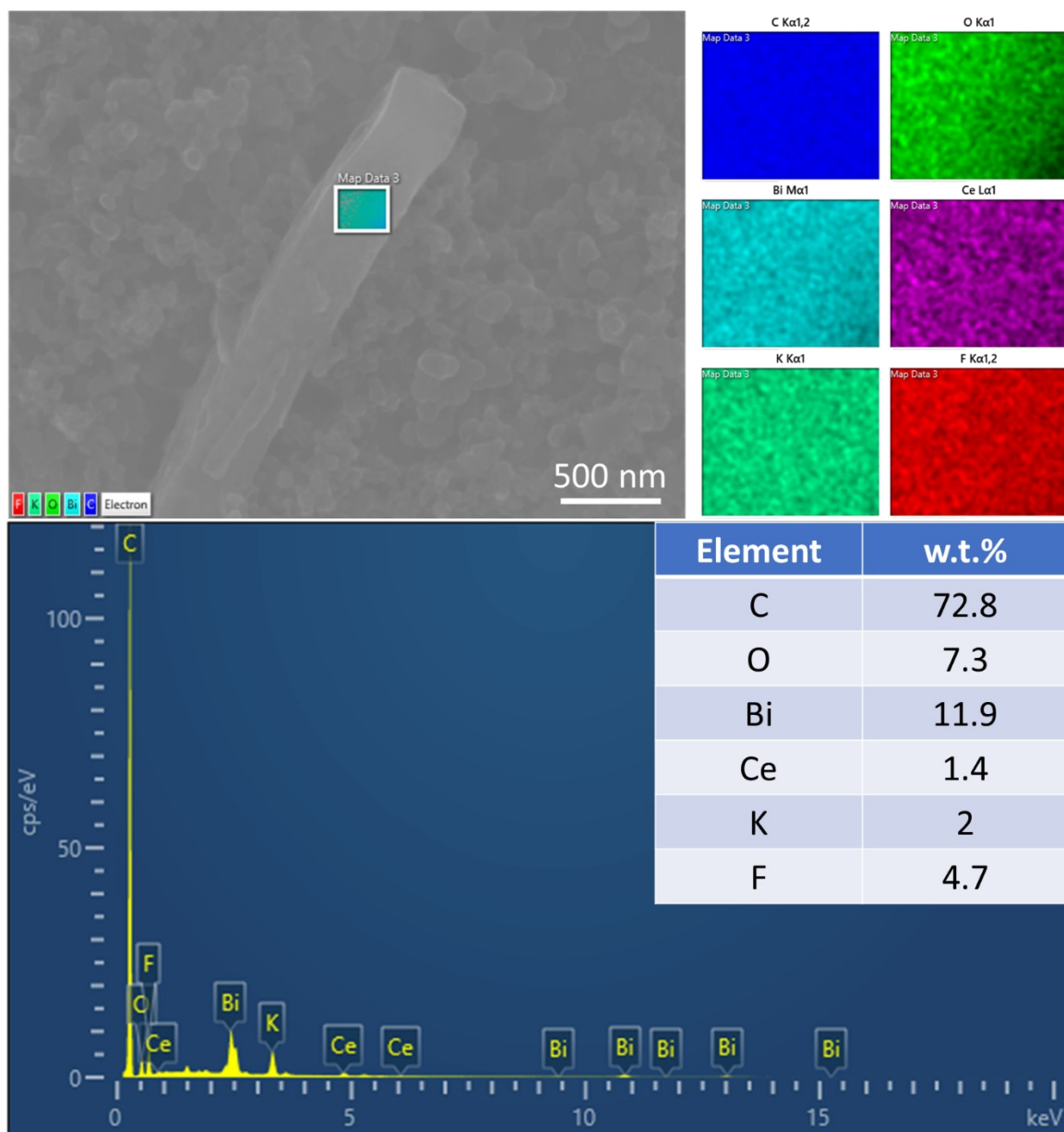
Figure S19. Elemental mapping of $Ce_{0.05}Bi_{0.95}@C$ NRs after stability test.

Table S1. Peak fitting results of Raman spectrum of (a) Bi@C NRs; (b) $Ce_{0.01}Bi_{0.99}$@C NRs; (c) $Ce_{0.05}Bi_{0.95}$@C NRs; (d) $Ce_{0.1}Bi_{0.9}$@C NRs.

Catalyst	I_D/I_G
Bi@C	2.237
$Ce_{0.01}Bi_{0.99}$@C	2.446
$Ce_{0.05}Bi_{0.95}$@C	2.670
$Ce_{0.1}Bi_{0.9}$@C	2.144

Table S2-1. Summary of Bi-based catalysts for formate production in CO_2RR (CO_2-saturated 0.1 M $KHCO_3$).

Catalyst	$FE_{formate}$	$j_{formate}$	Potential	Stability	Potential window
Bi/Sn [2]	94.8%	32 mA/cm^2	-1.0 V$_{vs. RHE}$	20 hrs	200 mV
Bi$_2$O$_3$@MCCM [3]	90%	17.7 mA/cm^2	-1.36 V$_{vs. RHE}$	12 hrs	300 mV
BiOx/C [4]	96%	12.5 mA/cm^2	-1.37 V$_{vs. RHE}$	0.5 hrs	350 mV
BiOBr [5]	95%	60 mA/cm^2	-0.9 V$_{vs. RHE}$	65 hrs	50 mV
Bi-Sn aero gel 6]	93.9%	9.3 mA/cm^2	-1.1 V$_{vs. RHE}$	10 hrs	200 mV
Bi NSs [7]	98%	16 mA/cm^2	-0.9 V$_{vs. RHE}$	100 hrs	400 mV
Bi/Cu [8]	100%	4 mA/cm^2	-1.5 V$_{vs. RHE}$	24 hrs	520 mV
Bi MSs [9]	96.2%	15 mA/cm^2	-1.0 V$_{vs. RHE}$	50 hrs	500 mV
BOC [10]	92.6%	35 mA/cm^2	-1.5 V$_{vs. RHE}$	8 hrs	300 mV
Bi NPs [11]	98%	21.6 mA/cm^2	-1.5 V$_{vs. RHE}$	20 hrs	500 mV
Bi-Cu [12]	94.1%	24.4 mA/cm^2	-1.0 V$_{vs. RHE}$	20 hrs	500 mV
Bi NTs [13]	97%	39.4 mA/cm^2	-1.1 V$_{vs. RHE}$	10 hrs	400 mV
5% Ce-doped B@C	96.1%	30.3 mA/cm^2	-1.5 V$_{vs. RHE}$	40 hrs	**1000 mV**

Table S2-2. Comparison of Highest $FE_{formate}$ with catalysts working in different conditions.

Catalyst	Electrolyte	Highest $FE_{formate}$
5% Ce-doped B@C	0.1 M $KHCO_3$	96.1%
Bi$_2$O$_3$@GO [14]	0.5 M $KHCO_3$	87.17%
MnO$_2$/g-C$_3$N$_4$ [15]	0.5 M $KHCO_3$	68.65%
ZnO/g-C$_3$N$_4$ [16]	0.5 M $KHCO_3$	87.17%
γ-Al$_2$O$_3$@rGO [17]	0.5 M $KHCO_3$	91.20%

References

1. Zheng, X., et al., *Sulfur-Modulated Tin Sites Enable Highly Selective Electrochemical Reduction of CO$_2$ to Formate.* Joule, 2017. **1**(4): p. 794-805.
2. Li, Z., et al., *Fabrication of Bi/Sn bimetallic electrode for high-performance electrochemical reduction of carbon dioxide to formate.* Chemical Engineering Journal, 2022. **428**.
3. Liu, S., et al., *Bi$_2$O$_3$ Nanosheets Grown on Multi-Channel Carbon Matrix to Catalyze Efficient CO(2) Electroreduction to HCOOH.* Angew Chem Int Ed Engl, 2019. **58**(39): p. 13828-13833.
4. Lee, C.W., et al., *Selective Electrochemical Production of Formate from Carbon Dioxide with Bismuth-Based Catalysts in an Aqueous Electrolyte.* ACS Catalysis, 2018. **8**(2): p. 931-937.
5. Garcia de Arquer, F.P., et al., *2D Metal Oxyhalide-Derived Catalysts for Efficient CO$_2$ Electroreduction.* Adv Mater, 2018. **30**(38): p. e1802858.
6. Wu, Z., et al., *Engineering Bismuth-Tin Interface in Bimetallic Aerogel with a 3D Porous Structure for Highly Selective Electrocatalytic CO$_2$ Reduction to HCOOH.* Angew Chem Int Ed Engl, 2021. **60**(22): p. 12554-12559.
7. Zhao, M., et al., *Atom vacancies induced electron-rich surface of ultrathin Bi nanosheet for efficient electrochemical CO$_2$ reduction.* Applied Catalysis B: Environmental, 2020. **266**.
8. Jiang, H., et al., *High-selectivity electrochemical CO$_2$ reduction to formate at low overpotential over Bi catalyst with hexagonal sheet structure.* Applied Surface Science, 2021. **541**.
9. Zhang, Y., et al., *Mass-transfer-enhanced hydrophobic Bi microsheets for highly efficient electroreduction of CO$_2$ to pure formate in a wide potential window.* Applied Catalysis B: Environmental, 2023. **322**.
10. Wang, Y., et al., *Sub-2 nm ultra-thin Bi$_2$O$_2$CO$_3$ nanosheets with abundant Bi-O structures toward formic acid electrosynthesis over a wide potential window.* Nano Research, 2021. **15**(4): p. 2919-2927.
11. Ma, X., et al., *Polymeric carbon nitride supported Bi nanoparticles as highly efficient CO$_2$ reduction electrocatalyst in a wide potential range.* J Colloid Interface Sci, 2022. **608**(Pt 2): p. 1676-1684.
12. Wang, M., et al., *Synergistic Geometric and Electronic Effects in Bi–Cu Bimetallic Catalysts for CO$_2$ Electroreduction to Formate over a Wide Potential Window.* ACS Sustainable Chemistry & Engineering, 2022. **10**(17): p. 5693-5701.
13. Fan, K., et al., *Curved Surface Boosts Electrochemical CO$_2$ Reduction to Formate via Bismuth Nanotubes in a Wide Potential Window.* ACS Catalysis, 2019. **10**(1): p. 358-364.
14. Mulik, B., et al., *Bismuth-Oxide-Decorated Graphene Oxide Hybrids for Catalytic and Electrocatalytic Reduction of CO$_2$.* Chemistry–A European Journal, 2020. **26**(40): p. 8801-8809.
15. Mulik, B., et al., *Highly efficient manganese oxide decorated graphitic carbon nitrite electrocatalyst for reduction of CO$_2$ to formate.* Catalysis Today, 2021. **370**(1): p. 104-113.
16. Mulik, B., et al., *Electrocatalytic and catalytic CO$_2$ hydrogenation on ZnO/g-C$_3$N$_4$ hybrid nanoelectrodes.* Applied Surface Science, 2021. **538**: p. 148120.
17. Mulik, B., et al., *Facile synthesis and characterization of γ-Al$_2$O$_3$ loaded on reduced graphene oxide forelectrochemical reduction of CO$_2$.* Sustainable Energy & Fuels, 2022. **6**: p. 5308.